Article

Not peer-reviewed version

Watching Alkaline Phosphatase Catalysis Through Its Vibrational Fingerprint

Margherita Tamagnini [†], Haoyue Jiang [†], Liana Klivansky, Carlos Bustamante, Alessandra Lanzara [*]

Posted Date: 28 November 2025

doi: 10.20944/preprints202511.2139.v1

Keywords: Fourier-transform infrared spectroscopy (FTIR); alkaline phosphatase (ALP); spectral analysis; p-nitrophenyl phosphate (PNPP); molecular fingerprinting

 doi:10.20944/preprints202511.2139.v1

Article

Watching Alkaline Phosphatase Catalysis Through Its Vibrational Fingerprint

Margherita Tamagnini [1,†], Haoyue Jiang [2,3,†], Liana Klivansky [4], Carlos Bustamante [1,5] and Alessandra Lanzara [3,6,7,*]

[1] Department of Molecular and Cell Biology, University of California, Berkeley, CA 94720, USA
[2] Applied Science Technology, University of California, Berkeley, CA 94720, USA
[3] Materials Sciences Division, Lawrence Berkeley National Laboratory, Berkeley, CA 94720, USA
[4] Molecular Foundry, Lawrence Berkeley National Laboratory, Berkeley, California 94720, USA
[5] Institute for Quantitative Biosciences (QB3), University of California, Berkeley, California 94720, USA
[6] Department of Physics, University of California, Berkeley, CA 94720, USA
[7] Kavli Nanoscience Energy Institute, University California, Berkeley, CA 94720, USA
* Correspondence: alanzara@lbl.gov
† These authors contributed equally to this work.

Abstract

Despite decades of structural and kinetic characterization, the full spectral molecular vibrations that accompany the catalysis in alkaline phosphatase (ALP) have remained largely unexplored. In this study, we combine in situ real-time attenuated total reflection Fourier-transform infrared (ATR-FTIR) measurements over a large energy range, to track the hydrolysis of p-nitrophenyl phosphate (PNPP) and inorganic phosphate (Pi) over a large range of enzyme concentrations. From the static spectra of the pure components (ALP, PNPP, PNP, Pi), we identify their characteristic vibrational frequencies and use them as reference points for the time resolved spectra. The reaction reveals a monotonic growth of the inorganic-phosphate band at 1077 cm^{-1}. At the highest alkaline-phosphatase concentration, we resolve two blue shifts in the nitro/aromatic region (1510 → 1518 cm^{-1}; 1494 → 1499 cm^{-1}), two red shifts in the fingerprint region (1345 → 1340 cm^{-1}; 1294 → 1290 cm^{-1}), and a splitting of the ~1592 cm^{-1} band into 1595 and 1583 cm^{-1}. In conclusion, by anchoring the time-resolved spectra to the static spectra of individual constituents, we were able to resolve the infrared readout of the enzymatic reaction, offering a generalizable approach for FTIR-based tracking of catalytic processes.

Keywords: Fourier-transform infrared spectroscopy (FTIR); alkaline phosphatase (ALP); spectral analysis; p-nitrophenyl phosphate (PNPP); molecular fingerprinting

1. Introduction

Alkaline phosphatase (ALP) is a key metalloenzyme involved in critical biochemical pathways, playing a key role in metabolism, bone mineralization and diagnostic [1–8]. It is also an important biomarker in bone and chronic kidney disease contexts [9–12]. Its functional importance drives the need for a deeper understanding of its molecular dynamics and substrate interactions. However, despite decades of biochemical and structural studies characterizing ALP's activity, including its enzymatic conversion of p-nitrophenyl phosphate (PNPP) to p-nitrophenol (PNP), crystallographic snapshots of catalytic intermediates and kinetic analysis under different PH and metal ion conditions [1,13–17], details of how ALP interacts with substrates under varying conditions and hence its molecular dynamics during catalysis remain unclear.

Fourier-transform infrared (FTIR) spectroscopy provides a powerful probe of enzymatic transformations, sensitive to bond vibrations in both substrates and protein backbones [18–23]. Previous studies have provided structural or kinetic insights, but comprehensive Fourier-transform

 doi:10.20944/preprints202511.2139.v1

infrared spectroscopy (FTIR)-based analysis of enzymatic processes like ALP activity is limited [24–26].

Indeed, most FTIR studies to date have primarily focused on the mid-infrared (mid-IR) region (typically 900–1800 cm^{-1}), which contains the characteristic amide I and II bands that report on protein secondary structure and the fingerprint vibrations associated with substrate and product functional groups.

In contrast, the low-frequency region (500–900 cm^{-1}) which reports on metal-ligand and phosphate-related modes, and the high-frequency range (2800–4000 cm^{-1}), which includes C–H, N–H, and O–H stretching modes, sensitive to hydration and hydrogen bonding, remain largely unexplored in ALP.

In this paper we utilize state of the art FTIR spectroscopy to monitor in situ the real time dynamics of the catalytic conversion of PNPP to PNP, by probing the full vibrational spectra, from 500 to 4000 cm^{-1}. This allows us to capture both the conventional mid-IR structural markers and the underexplored low- and high-frequency features, providing a more holistic view of the molecular environment, secondary structure, metal-center interactions of ALP and its catalytic function. This approach complements kinetic and crystallographic studies by providing a continuous spectroscopic fingerprint of catalysis under near-native aqueous conditions.

2. Materials and Methods

All experiments were performed under controlled aqueous conditions using full-range attenuated total reflection FTIR to monitor ALP-catalyzed PNPP hydrolysis in real time.

2.1. Materials

Alkaline phosphatase (ALP) and its corresponding assay buffer were prepared and provided by the Bustamante laboratory. The ALP sample was originally expressed and purified following the procedures described in Chen et al., PNAS 2020 (117, 24740–24748). *E. coli* alkaline phosphatase (PhoA) was purified under native conditions and supplied in buffer containing 20 mM Tris–HCl (pH 8.0) and 100 mM NaCl, without added divalent cations. The enzyme stock was stored on ice and diluted to the desired concentration immediately before each measurement. All other chemicals, including p-nitrophenyl phosphate (PNPP, Cat. No. 34045), p-nitrophenol (PNP, Cat. No. 1048), and inorganic phosphate (Pi, Cat. No. 10385405), were purchased from Thermo Scientific (Waltham, MA, USA) and used without further purification. All aqueous solutions were prepared using ultrapure water (18.2 MΩ·cm) and the same 20 mM Tris·HCl (pH 8.0) and 100 mM NaCl.

2.2. Sample Preparation

For the static FTIR experiments, four reference solutions were prepared: 20 μM ALP, 610 mM PNPP, 115 mM PNP, and 183 mM Pi. All solutions were dissolved in the same buffer described above. The concentrations of ALP, PNPP, PNP, and Pi were individually adjusted to optimize the FTIR signal for each species, yielding comparable peak intensities while accounting for their distinct infrared absorption cross-sections, solubility limits, and molecular sizes.

For the time-resolved (reaction) experiments, ALP and PNPP stock solutions (20 μM and 608 mM, respectively) were mixed directly on the ATR crystal in equal volumes (5 μL + 5 μL) of the two solutions to yield a 10 μL reaction mixture containing 10 μM ALP and 305 mM PNPP. This configuration allowed us to initiate and monitor the enzymatic hydrolysis of PNPP in situ, providing a continuous spectral record of product formation and substrate consumption. Additional mixtures were prepared by varying the ALP and PNPP concentrations to obtain (i) a high-ALP condition (10 μM ALP, 61 mM PNPP) and (ii) a low-ALP condition (1 μM ALP, 305 mM PNPP). All solutions were freshly prepared in the same buffer immediately before each measurement and maintained at PH 8. The pH remained stable during mixing and reaction, as the added enzyme and substrates had negligible buffering capacity compared with the Tris buffer used throughout this study.

 doi:10.20944/preprints202511.2139.v1

2.3. FTIR Measurements

All FTIR measurements were performed at 295 ± 2 K using a Nicolet iS50 spectrometer (Thermo Scientific) equipped with a diamond ATR accessory. Figure 1(a) illustrates the ATR-FTIR optical layout, sampling geometry, together with the data processing sequence from interferogram to absorbance spectra. In the Michelson interferometer, a KBr beamsplitter splits the broadband IR beam into a fixed-mirror arm and a moving-mirror arm; their recombination produces a multiplexed interferogram that is Fourier-transformed into a spectrum. In ATR, the beam undergoes total internal reflection in the diamond, generating an evanescent field that samples approximately 1–2 μm of the droplet before reaching the DTGS detector.

The spectrometer was routinely wavenumber-calibrated with a standard polystyrene film to ensure spectral accuracy. Spectra were collected over 400–4000 cm^{-1} at a resolution of 4 cm^{-1}. Data spacing was 0.25 cm^{-1} for static spectra and 0.5 cm^{-1} for time-resolved acquisitions. Prior to each measurement, an instrument background spectrum was recorded with a clean, dry ATR crystal to calibrate the detector response. A buffer background was collected at the beginning of each session (one for the static data day and one for the time-resolved day), and the corresponding session background was used for that session's measurements. Approximately 10 μL of sample was deposited on the ATR crystal for each static measurement.

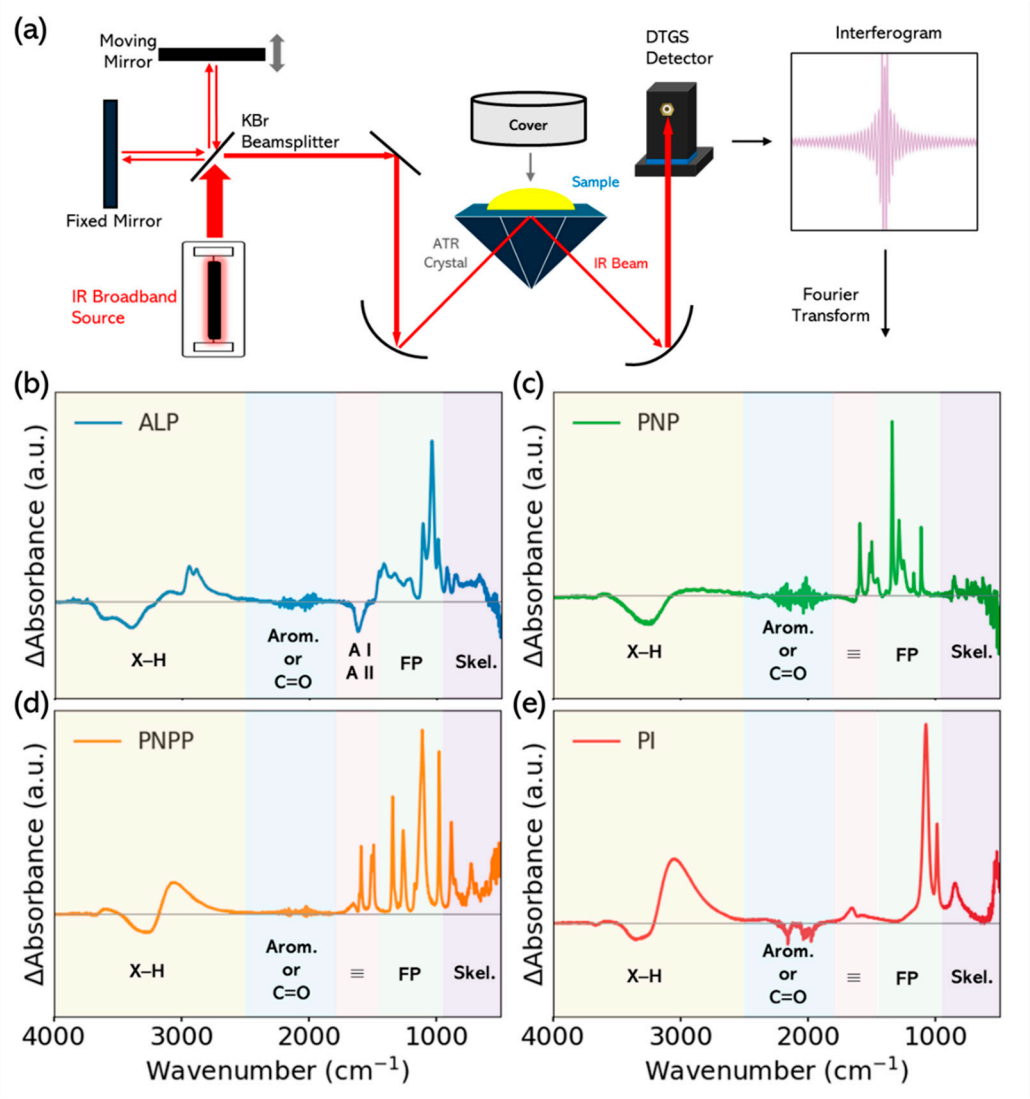

Figure 1. ATR-FTIR layout and reference spectra. (**a**) A broadband SiC ("Globar") source is split by a KBr beamsplitter into the fixed- and moving-mirror arms of a Michelson interferometer; recombination produces a

 doi:10.20944/preprints202511.2139.v1

time-dependent interferogram that is Fourier transformed to yield spectra. During measurement, the droplet on the diamond ATR was covered to limit evaporation and atmospheric H_2O/CO_2 pickup. Total internal reflection generates an evanescent field that probes ~1–2 μm of the sample before detection by the DTGS (KBr) detector. (b–e) Reference ATR-FTIR spectra of the individual components: (**b**) ALP (20 μM; pH 8 buffer), (**c**) PNP (115 mM), (**d**) PNPP (610 mM), (**e**) Pi (183 mM). Spectra were recorded on a Nicolet iS50 (diamond ATR, KBr beamsplitter, DTGS detector) over 500–4000 cm^{-1} at 4 cm^{-1} resolution; air served as the background and the buffer spectrum was subtracted.

For the static spectra, 256 scans were averaged per acquisition to maximize signal-to-noise. The ATR micro-well was left open (no lid), so the droplet was exposed to ambient air.

For the time-resolved experiments, 64 scans were averaged per spectrum to balance acquisition speed and spectral quality, yielding <1 min per spectrum and a temporal resolution of 1.5 min. The reaction was initiated by manually mixing ALP and PNPP solutions directly on the ATR crystal for approximately 10 s. The ATR micro-cell was then sealed to minimize evaporation, using the iS50 ATR liquid holder volatile cover (Thermo Scientific, P/N 470-470300). Time zero (t = 0) was defined as the start of acquisition.

All measurements were performed at constant pH 8.0 ± 0.1, corresponding to the optimal catalytic condition of ALP. Spectra were acquired using OMNIC software (Thermo Scientific) and further processed in Python (v3.10.18) for subsequent analysis and visualization.

2.4. Data Analysis

All FTIR spectra were processed and analyzed using custom in-house Python scripts. Raw absorbance spectra were first corrected for baseline drift and buffer contribution by subtracting the corresponding blank spectrum measured under identical conditions.

Quantitative analysis was performed by fitting predefined spectral windows with standard Voigt line-shape model (Gaussian σ and Lorentzian γ) plus a linear baseline. A single-peak Voigt model was used by default. Two- or three-Voigt component fits were applied only where derivative inspection or residual analysis indicated partial overlapping components. Initial parameters were estimated from lightly smoothed spectra using a Savitzky–Golay filter (2nd order, 5 –10 points) to assist derivative-based peak detection; this step was used solely for initialization and not for quantitative fitting or presentation.

For static reference spectra (ALP, PNPP, PNP, and Pi), peak centers were freely fitted within broad physically reasonable ranges (typically ±20–30 cm^{-1} from literature values). These fitted positions were then used as references values to constrain the corresponding peaks in the time-resolved series (±5–10 cm^{-1}). All fits were performed using bounded non-linear least squares with non-negative amplitudes, center positions constrained with ±5–10 cm^{-1} of the reference values from static spectra, and Gaussian/Lorentzian widths limited to physically reasonable ranges (σ = 1–15 cm^{-1}, γ = 1–20 cm^{-1}) to prevent overfitting. Fit quality was verified by residual analysis, and fits showing systematic deviations were manually reviewed.

For time-resolved FTIR measurements, each time slice of the reaction series was analyzed independently following the same baseline correction and windowed Voigt-fitting workflow described above. The resulting spectra were then compared through direct spectral tracking and derivative-based differential analysis, as detailed in the Results section.

3. Results

3.1. Static Absorbance of ALP, PNPP, PNP and Pi

The first step to understand the real time dynamics of the catalytic conversion is to study the full vibrational spectra, in static conditions, of each of its constituents.

 doi:10.20944/preprints202511.2139.v1

Figure 1 (b-e) report the static FTIR–ATR spectra of ALP, PNPP, PNP, and Pi. The spectra can be divided into five characteristic regions including X-H vibrations, aromatic/C=O vibrations, amides modes, phosphate modes, and skeletal region.

Panel b shows the FTIR–ATR spectrum of ALP (20 μM, pH 8 buffer, RT), revealing the typical broad and complex vibrational pattern of a folded protein, characterized by a broad band in the high-frequency region (X–H stretching), strong amide bands between 1700–1500 cm^{-1}, and multiple peaks in the fingerprint range (1200–900 cm^{-1}) arising from side-chain and phosphate vibrations. These features reflect contributions from backbone modes (Amide A, I, II, III), aliphatic C–H stretches, and phosphate-associated bonds, characteristics of glycoproteins.

By comparing observed wavenumbers to standard infrared reference tables [27–30], protein spectroscopy reviews [18,31,32], and published FTIR analyses of amide and phosphate vibrations [28,30,33], we can assign the following modes to each peak in the spectra.

In the high-frequency X-H region (4000-2500 cm^{-1}), the broad peak near 3398 cm^{-1} corresponds to Amide A (N–H stretching), sensitive to hydrogen bonding within the protein backbone [18,31,32], while the two weaker features at 2944 and 2889 cm^{-1} are assigned to alkyl C–H stretches from protein side chains [27,34].

In the Amide I region between 1700–1620 cm^{-1} we distinguish multiple peaks. The peak near 1708 cm^{-1} is attributed to β-turn structures (C=O stretching, hydrogen-bonded) [18,35], while the peak at 1624 cm^{-1} arises from intermolecular β-sheet arrangements [18,31]. These Amide I peaks primarily reflect C=O stretching coupled to CN and NH modes and provide insights into secondary structure.

In the Amide II region, the peaks at 1551 and 1531 cm^{-1} correspond to the Amide II band, dominated by N–H in-plane bending and C–N stretching, with contributions from C=O bending [18,31,33]. Although these peaks are mainly associated with the peptide bond vibrations, they also provide information on hydrogen bonding.

In the Mid-frequency side-chain region (1500–1200 cm^{-1}), the peak at 1459 cm^{-1} is assigned to CH_2 scissoring vibrations [27,36], and the nearby peak at 1418 cm^{-1} to symmetric COO^- stretching, indicative of carboxylate groups in acidic residues [37]. A weaker mode at 1334 cm^{-1} can be resolved and is associated with the CH_2 wagging vibrations [27,38].

The strongest contribution to the FTIR spectra is observed in the amide III region (1300-1200 cm^{-1}), where the strong peak at 1215 cm^{-1} arises from coupled N–H bending and C–N stretching vibrations. This band is strongly hydrogen-bond sensitive, and its position is directly related to the backbone conformation [18,31,32].

Phosphate/carbohydrate region (1200–900 cm^{-1}): Several strong peaks appear in the 1100–900 cm^{-1} range. The band at 1112 cm^{-1} is consistent with symmetric PO_2^- stretching and possible carbohydrate C–O vibrations [30]. A peak at 1043 cm^{-1} reflects carbohydrate C–O/C–O–C contributions, overlapping with phosphate [30]. The band at 994 cm^{-1} corresponds to phosphate ν_1 (symmetric P–O stretch, mono-/diesters) [28]. Finally, the 923 cm^{-1} band is attributed to P–O–P asymmetric stretching (bridging phosphate) or phosphoryl OH vibrations [39].

This complexity reflects the enzyme's glycoprotein nature, its secondary structure content, and the importance of phosphate interactions in catalysis.

A consolidated list of observed bands and their assignments is provided in Table 1.

Table 1. Peak positions and assignments in the ALP FTIR–ATR spectrum. Observed maxima (cm^{-1}), bond assignments, and functional group vibrations are listed.

Peak position (cm^{-1})	Assignment	Bond description
3398	Amide A	N–H stretching (hydrogen-bond sensitive)
2944	C–H stretch	Alkyl side chains
2889	C–H stretch	Alkyl side chains
1708	Amide I (β-turn)	C=O stretching + H-bonding
1624	Amide I (β-sheet)	C=O stretching, intermolecular β-sheet

 doi:10.20944/preprints202511.2139.v1

1551	Amide II	NH bending + CN stretching
1531	Amide II	NH bending + CN stretching
1459	CH_2 scissoring	CH_2 bending vibrations
1418	COO^- symmetric stretch	Carboxylates
1334	CH_2 wagging	Side-chain CH_2 vibration
1215	Amide III	NH bending + CN stretching (H-bond sensitive)

Panels (c-e) show the FTIR spectra of PNPP, PNP and PI. Contrarily to ALP, which reveals broad amide bands (Amide I and II) between 1500–1700 cm^{-1} and complex multiplets in the fingerprint region, PNPP, PNP, and Pi exhibit narrow peaks concentrated mainly between 1800–900 cm^{-1}, consistent with their reduced chemical complexity. In the high-frequency region (4000–2800 cm^{-1}), only PNP reveals a broad O–H band, while PNPP and Pi remain largely featureless, providing a distinct spectral handle for identifying the reaction product.

All peak identifications were derived from experimental spectral databases [40–42] and from established group-frequency compilations [30,43,44].

Panel c shows the spectrum of PNP, which reveals how, after hydrolysis, the product retains aromatic ring modes, with C=C stretching near 1600 cm^{-1} and a broad O–H band at 3200–3600 cm^{-1}, reflecting the phenolic hydroxyl group [44,45]. The persistence of NO_2 peaks (1330 and 1520 cm^{-1}), albeit shifted, highlights change in the electronic environment due to the removal of the phosphate group [40,43]. These spectral differences between PNPP and PNP provide a molecular fingerprint of the enzymatic reaction outcome. The combined appearance of the O–H band and slight downshift of the NO_2 doublet serve as direct evidence of phosphate cleavage and phenolic product formation.

Panel d shows the spectrum of PNPP displays strong nitro group vibrations at 1330 and 1520 cm^{-1}, corresponding to symmetric and asymmetric NO_2 stretching. These peaks are diagnostic of aromatic nitro compounds and are sensitive to the electronic environment [40,43,44]. Additionally, phosphate-related P–O vibrations appear around 850–1100 cm^{-1}, consistent with the presence of a phosphate ester group [30]. These bands are particularly important because they diminish during ALP-catalyzed hydrolysis, serving as spectral markers of substrate consumption. The phosphate-ester vibrations are vividly distinct from the aromatic and nitro regions, allowing unambiguous tracking of PNPP depletion during the catalysis reaction.

The Pi spectra is shown on panel e. The Pi spectrum exhibits strong, sharp bands between 900–1200 cm^{-1}, corresponding to symmetric and asymmetric P–O and P=O stretching vibrations [29,39,46,47]. These modes serve as clear markers of phosphate release during ALP catalysis. A broad O–H stretching envelope (3000–3700 cm^{-1}) and a H_2O bending mode near 1655 cm^{-1} reveal hydration of the $H_2PO_4^-$/HPO_4^{2-} species [44]. The relative simplicity of the Pi spectrum, compared to PNPP and PNP, makes it a reliable indicator of reaction completion and product accumulation. Compared to PNPP and PNP, the Pi spectrum lacks aromatic bands entirely and has sharp phosphate vibrations, making it a clean reference for observing free phosphate accumulation.

3.2. In Situ Spectra of PNPP Reaction Under High ALP

Upon mixing alkaline phosphatase with p-nitrophenyl phosphate, time-resolved Fourier-transform infrared spectra were collected to monitor the reaction progress (Figure 2). The absorbance map in Figure 2b summarizes the full time evolution (red = higher absorbance, blue = lower), with time zero defined by the onset of mixing and sealing. Selected bands increase or decrease depending on whether they report product formation or substrate depletion.

 doi:10.20944/preprints202511.2139.v1

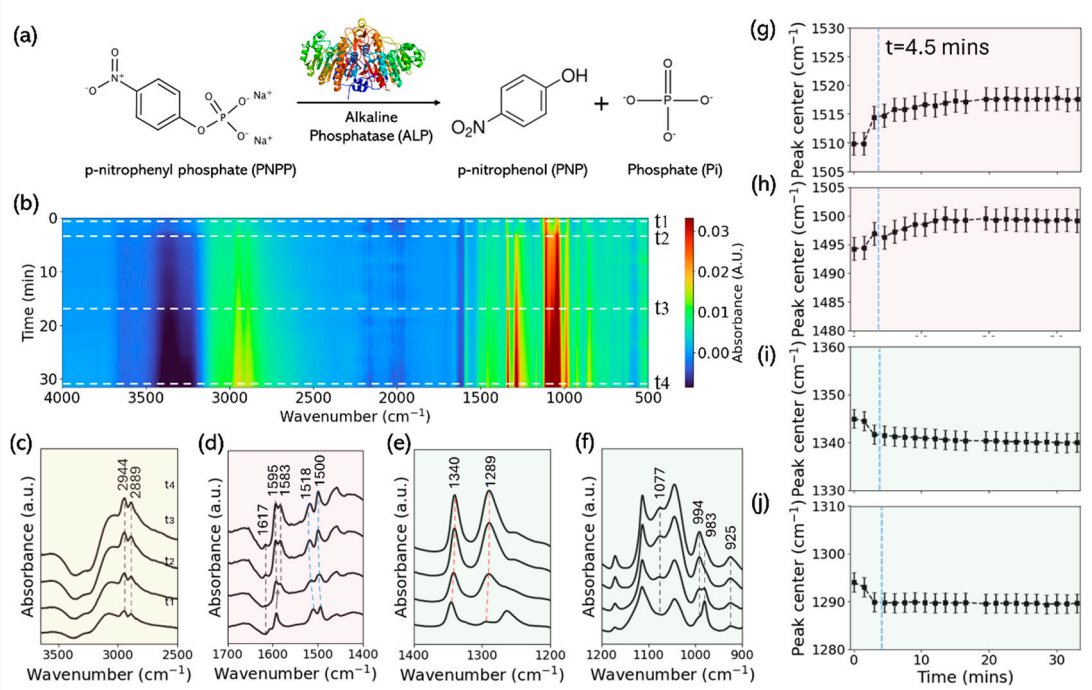

Figure 2. ALP-catalyzed PNPP hydrolysis monitored by ATR-FTIR (high [ALP] dataset). (a) Reaction scheme. (b) In-situ absorbance map (500–4000 cm^{-1}) with four time cuts marked by horizontal dashed lines (t_1–t_4 = 0, 4.5, 25.5, 33 min); dashed rectangles indicate analysis windows. (c–f) Spectral snapshots at t_1–t_4 from the same run in three windows: (c) C–H stretching (≈3500–2500 cm^{-1}); (d) nitro/aromatic region (1700–1400 cm^{-1}) highlighting the emergence of a doublet near ~1592 cm^{-1} that resolves into 1595 and 1583 cm^{-1} at late times, together with blue-shifting bands at 1510 → 1518 cm^{-1} and 1494 → 1499 cm^{-1}; (e) fingerprint-I (1400–1200 cm^{-1}) showing red shifts 1345 → 1340 cm^{-1} and 1294 → 1290 cm^{-1}; (f) fingerprint-II / phosphate window (1115–900 cm^{-1}) showing monotonic growth of the inorganic-phosphate band near 1077 cm^{-1}. (g–j) Peak-center trajectories for the four tracked modes corresponding to the windows in (d–e): (g) 1510 → 1518 cm^{-1} (blue shift), (h) 1494 → 1499 cm^{-1} (blue shift), (i) 1345 → 1340 cm^{-1} (red shift), (j) 1294 → 1290 cm^{-1} (red shift). The vertical dashed line at t ≈ 4.5 min in (g–j) marks the time at which kinetic fits to the 1077 cm^{-1} Pi band indicate that the reaction has effectively reached completion.

In the aromatic/nitro window (1700–1400 cm^{-1}), two reproducible changes are resolved in the time cuts (Figure 2d). First, within 1600–1620 cm^{-1} the feature that visually appears to drift is explained by intensity redistribution between two overlapping components near ~1606 and ~1617 cm^{-1}: the p-nitrophenyl-phosphate–related mode (~1606 cm^{-1}) decreases while the p-nitrophenol–related mode (~1617 cm^{-1}) grows, with fitted centers remaining essentially constant within uncertainty. Second, the envelope near ~1592 cm^{-1} resolves into a doublet at ~1595 and ~1583 cm^{-1} that remains visible at the latest time cut (t_4). In addition, small blue shifts are observed for the ~1510 → ~1518 cm^{-1} and ~1494 → ~1499 cm^{-1} components. In the static references, p-nitrophenyl phosphate (~1591 cm^{-1}) and p-nitrophenol (~1595 cm^{-1}) delimit this aromatic C=C region, whereas alkaline phosphatase and inorganic phosphate show no isolated features there; the 1510/1495 cm^{-1} pair lies in the nitro window of the substrate/product with only limited influence from the alkaline-phosphatase amide-II envelope (Section 3.1).

In the fingerprint range, the trends align with the inorganic-phosphate and p-nitrophenyl-phosphate references (Figure 2e,f). The 1077 cm^{-1} band increases monotonically toward a plateau, matching the inorganic-phosphate marker identified in Section 3.1; the ~990 cm^{-1} region is not used as a primary readout because it overlaps with the alkaline-phosphatase ~925 cm^{-1} band and the long tail of inorganic-phosphate ~847 cm^{-1}. Within 1400–1200 cm^{-1}, the ~1345 → ~1340 cm^{-1} and ~1294 → ~1290 cm^{-1} bands exhibit small red shifts that reside in the substrate-side window, while alkaline phosphatase contributes only weak CH_2/carbohydrate features around ~1334 cm^{-1} and inorganic

 doi:10.20944/preprints202511.2139.v1

phosphate has no strong modes there. As a stability check, the 1460 cm^{-1} CH_2 scissoring band (present in alkaline phosphatase and p-nitrophenol) shows negligible center motion.

Quantified trajectories for the four tracked centers are shown in Figure 2g–j, confirming two blue shifts (1510 → 1518 cm^{-1}; 1494 → 1499 cm^{-1}) and two red shifts (1345 → 1340 cm^{-1}; 1294 → 1290 cm^{-1}) that evolve smoothly toward steady values under the high-concentration condition; fitting and normalization procedures are described in Methods.

3.3. ALP Concentration-Dependence

We also quantified peak centers over time at low, intermediate, and high [ALP] (Methods). Figure 3 assembles these datasets to highlight how the structural response scales with enzyme loading. The time–wavenumber maps for the three concentrations (Figure 3a–c) show similar overall evolution in the 1700–900 cm^{-1} region, but the amplitude of the changes in the aromatic and fingerprint windows clearly decreases from high to mid to low [ALP]. Normalized spectra taken at t = 0 and 33 min in two structural windows (1250–1350 and 1050–1150 cm^{-1}; Figure 3d–g) make this trend more explicit. At t = 0 min all three traces share the same set of bands and very similar peak positions, with only modest intensity differences that reflect the varying amount of ALP in the mixture. By t = 33 min, however, the high-[ALP] spectra show the strongest reshaping: in the 1250–1350 cm^{-1} window (Figure 3e) the two PNPP fingerprint features near 1345 and 1294 cm^{-1} are strongly redistributed and slightly shifted, whereas in the 1050–1150 cm^{-1} window (Figure 3g) the emerging inorganic-phosphate band near 1077 cm^{-1} produces a pronounced low-frequency shoulder on the PNP band. The mid-[ALP] spectra follow the same qualitative pattern with reduced magnitude, and the low-[ALP] spectra remain much closer to their t = 0 min profiles, with only a modest Pi shoulder and limited distortion of the fingerprint envelope.

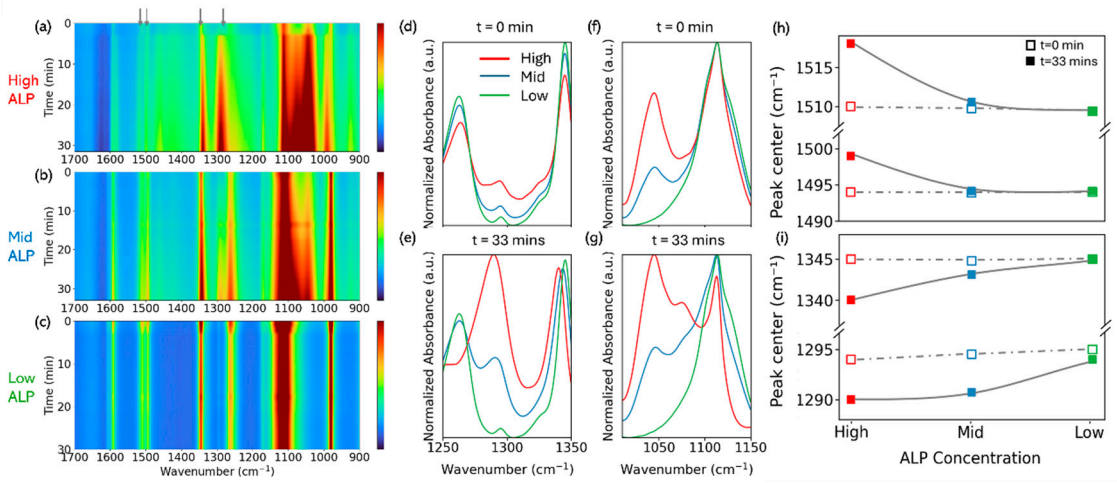

Figure 3. (a–c) Time–wavenumber ATR–FTIR maps for high, mid, and low ALP concentrations, respectively, showing the evolution of the PNPP/PNP/Pi region over 0–33 min. Gray arrows in (a) mark the four bands whose kinetics are analyzed in the subsequent panels. (d–g) Normalized absorbance spectra at selected windows for the three ALP concentrations (red = High, blue = Mid, green = Low). Panels (d) and (f) show the initial spectra at t = 0 min, while panels (e) and (g) show the corresponding spectra at t = 33 min, highlighting concentration-dependent band shapes and shifts in the fingerprint regions. (h–i) Peak center positions extracted from Voigt fits for the aromatic C=C/NO_2 pair (h) and the PNPP fingerprint-I / II pair (i) as a function of ALP concentration. Open squares denote initial positions at t = 0 min and filled squares denote final positions at t = 33 min; gray dashed lines connect the t = 0 min peak centers across ALP concentrations and serve as a visual reference for the subsequent shifts.

These qualitative trends are captured more compactly by the peak-center analysis in Figure 3h,i. At the initial time, all four markers have the same centers within our resolution—approximately 1510,

 doi:10.20944/preprints202511.2139.v1

1494, 1345, and 1294–1295 cm^{-1}—so the dashed gray lines connecting the t = 0 min points are essentially flat across [ALP]. Subsequent motion, however, scales strongly with concentration. In the nitro/aromatic window, the band near 1510 cm^{-1}—assigned to a mode in the NO_2/aryl C=C region—blue-shifts to 1518 cm^{-1} at high enzyme concentration ($\Delta\nu$ = +8 cm^{-1}), while at mid concentration it moves only to 1510.542 cm^{-1} ($\Delta\nu$ = +0.80 cm^{-1}) and at low concentration it is unchanged within resolution (1509.4 → 1509.4 cm^{-1}). Its companion near 1494 cm^{-1}—also within the NO_2-coupled aromatic manifold—blue-shifts to 1499 cm^{-1} at high concentration ($\Delta\nu$ = +5 cm^{-1}), but only +0.30 cm^{-1} at mid concentration (1493.9 → 1494.2 cm^{-1}) and +0.18 cm^{-1} at low concentration. In the fingerprint-I window, the ~1345 cm^{-1} marker—dominated by sym $\nu(NO_2)$ with contributions from phenolic ν(C–O)—red-shifts to 1340 cm^{-1} at high concentration ($\Delta\nu$ = −5 cm^{-1}), shows a smaller change at mid concentration (1344.8 → 1343.1 cm^{-1}; $\Delta\nu$ = −1.7 cm^{-1}), and exhibits no resolvable shift at low concentration (1345 → 1345 cm^{-1}). The ~1294–1295 cm^{-1} marker—assigned to a phenolic C–O / substrate-side fingerprint mode—red-shifts to 1290 cm^{-1} at high concentration ($\Delta\nu$ = −4 cm^{-1}), to 1290.7 cm^{-1} at mid concentration ($\Delta\nu$ = −3.8 cm^{-1}), and changes only slightly at low concentration (1295 → 1294 cm^{-1}; $\Delta\nu$ = −1 cm^{-1}). Together, the spectral slices in Figure 3d–g and the peak-center summary in Figure 3h,i show that two nitro/aromatic modes blue-shift and two substrate-side fingerprint modes red-shift, with shift amplitudes that diminish systematically from high to mid to low enzyme concentration, while all four centers share common starting positions across the series.

4. Discussion

Static spectra of alkaline phosphatase, p-nitrophenyl phosphate, p-nitrophenol, and inorganic phosphate provide the reference framework for three robust time-resolved outcomes in our in-situ series: clean product growth at 1077 cm^{-1}, a structured evolution in the ~1590–1620 cm^{-1} aromatic window, and small red shifts in the 1400–1200 cm^{-1} fingerprint region. The 1077 cm^{-1} band is strong and comparatively isolated in the phosphate spectrum, whereas the ~990 cm^{-1} phosphate band lies in a region lifted by the protein (~923–925 cm^{-1}) and the broad phosphate feature near ~847 cm^{-1}. Consistent with this, the 1077 cm^{-1} trajectory rises monotonically toward a plateau across enzyme concentrations and serves as the primary product readout (Figure 2; Methods).

In the aromatic window under high enzyme loading, two reproducible observations emerge. The envelope near ~1592 cm^{-1} resolves at late times into a ~1595/1583 cm^{-1} doublet, while the feature that visually appears to drift within 1600–1620 cm^{-1} is accounted for by time-dependent intensity redistribution between two overlapping components near ~1606 and ~1617 cm^{-1}; within fit uncertainty, the component centers themselves remain essentially stationary. Static references place p-nitrophenyl phosphate near ~1591 cm^{-1} and p-nitrophenol near ~1595 cm^{-1}, so the resolved doublet may reflect the coexistence of substrate-like and product-like environments; a minor phenolate-like contribution near 1595 cm^{-1} is compatible with product buildup and small adjustments in aromatic conjugation. Alternatively, local binding or electrostatic heterogeneity could produce minor vibrational splitting without chemical change. Small blue shifts of the ~1510 → ~1518 cm^{-1} and ~1494 → ~1499 cm^{-1} features fall within the nitro/aromatic manifold and likely report modest adjustments in local electrostatics, hydrogen-bonding networks, or ionization equilibria rather than wholesale changes of normal-mode identity.

In the fingerprint-I window, the ~1345 → ~1340 cm^{-1} and ~1294 → ~1290 cm^{-1} markers exhibit small but consistent red shifts under high enzyme loading. Because these bands sit in the substrate-side fingerprint region, their evolution can arise from composition-driven centroid changes as substrate is replaced by product, from gradual reorganization of solvation and hydrogen-bond networks around the nitro/phenoxide system, and from weak protein-side contributions around ~1334 cm^{-1}. Such red shifts are in line with minor relaxation of C–O and P–O bonds after PNPP cleavage and with the increased charge delocalization linked with phenolate accumulation. We therefore use these bands primarily as structural reporters rather than as the principal quantitative channel.

 doi:10.20944/preprints202511.2139.v1

A consistent concentration dependence is observed when comparing high, mid, and low enzyme loadings (Figure 3). The initial peak centers are indistinguishable within resolution across conditions, indicating that the starting vibrational landscape is independent of enzyme concentration. By contrast, the amplitudes of the subsequent shifts decrease monotonically with decreasing enzyme concentration and, at the lowest loading, fall below detectability. This behavior can be rationalized without invoking a single specific mechanism: deeper conversion within the fixed 33-min acquisition window produces larger composition-weighted centroid changes in overlapping bands; higher site occupancy at high loading amplifies local field and hydrogen-bond perturbations associated with binding; slower apparent kinetics at low loading reduce the net change observable within the time window; and the combination of signal-to-noise and residual drift compensation imposes a finite detection threshold for small shifts (0–8 cm^{-1}).

Controls and limitations were implemented to avoid conflating thickness or carrier effects with chemical shifts. The 1460 cm^{-1} CH_2 scissoring band, present in protein and p-nitrophenol, is thickness-sensitive and is therefore used as a stability check rather than for normalization. The protein-associated band near ~1045 cm^{-1} remains comparatively stable in center and width, and the ~925 cm^{-1} band is robust at high and mid enzyme loadings but often falls below detectability at low loading. For the ~1590–1620 cm^{-1} window, the main text reports the spectral bounds and time courses, while the Supplementary Information compares fixed-center and free-center fits (residuals and AIC/BIC) to substantiate the intensity-redistribution interpretation and to document plausible alternatives such as binding-mode heterogeneity or coupling changes.

Taken together, the static-anchored analysis yields a compact and reproducible infrared readout of turnover and structural evolution: 1077 cm^{-1} tracks product formation; the ~1590–1620 cm^{-1} region reports a structured development that includes late-time doublet resolution and intensity redistribution between overlapping modes; and 1345/1294 cm^{-1} capture small substrate-side red shifts. The amplitudes of these changes diminish systematically with decreasing enzyme concentration, whereas the starting frequencies are common across conditions. Future experiments that vary ionic strength and pH, implement solvent-isotope substitution, or use competition/site-blocking assays—ideally combined with polarization- or orientation-sensitive ATR measurements—should help to disentangle composition changes from microenvironment and binding effects within the same static–dynamic framework.

5. Conclusions

This study demonstrates the capability of full-range, time-resolved FTIR spectroscopy to monitor in situ the catalytic conversion of PNPP to PNP by ALP across the entire 500–4000 cm^{-1} range. Static spectra of the pure components, ALP, PNPP, PNP, and PI, provided the essential vibrational framework that enabled clear differentiation of substrate, product, and enzyme contributions. By integrating static references, and time-resolved tracking, this workflow yields a compact yet information-rich readout of enzymatic turnover.

These references anchored quantitative tracking of spectral evolution during catalysis and ensured robust deconvolution of overlapping modes.

In the reaction series, the 1077 cm^{-1} phosphate stretch emerged as a reliable marker of product formation, rising monotonically to a plateau under all enzyme concentrations. The aromatic region (1580–1620 cm^{-1}) revealed a structured evolution consistent with substrate-to-product transition: a doublet near 1583/1595 cm^{-1} appeared and a smaller shift in the nitro band near 1510 cm^{-1}. These trends capture subtle electronic and bonding rearrangements of the p-nitrophenyl group accompanying hydrolysis. Meanwhile, small but reproducible red shifts in the PNPP fingerprint-I window (1294 → 1290 cm^{-1}, 1345→1340 cm^{-1}) reflected progressive substrate depletion and possible weak coupling to enzyme-side vibrations.

Beyond establishing a framework for ALP, the approach offers a broadly generalizable strategy for decoding enzyme–substrate interactions through full-range FTIR, linking kinetic progress with molecular-level structural evolution.

 doi:10.20944/preprints202511.2139.v1

Supplementary Materials: The following supporting information can be downloaded at the website of this paper posted on Preprints.org.

Funding: A.L. acknowledges support from the Gordon and Betty Moore Foundation EPiQS Initiative through grant no. GBMF4859.

Institutional Review Board Statement: Not applicable.

Informed Consent Statement: Not applicable.

Data Availability Statement: The data presented in this study are available on request from the corresponding author.

Acknowledgments: The authors thank the Bustamante laboratory for providing the alkaline phosphatase (ALP) and buffer materials, especially Zhijie Chen for preparing the purified ALP samples, and Hailan Luo in the Lanzara group for valuable discussions and technical support. The authors also thank Shannon Yan and Luca Moreschini for their helpful discussions and assistance during the early stages of this project. Work at the Molecular Foundry was supported by the Office of Science, Office of Basic Energy Sciences, of the U.S. Department of Energy under Contract No. DE-AC02-05CH11231.

References

1. Coleman, J.E. Structure and Mechanism of Alkaline Phosphatase. *Annual Review of Biophysics and Biomolecular Structure* 1992, *21*, 441–483. DOI: 10.1146/annurev.bb.21.060192.002301
2. Harris, H. The Human Alkaline Phosphatases: What We Know and What We Don't Know. *Clinica Chimica Acta* 1990, *186*, 133–150. DOI: 10.1016/0009-8981(90)90031-m
3. Harris, H. The Harvey lectures: series 76. Academic Press: New York, 1986; pp. 95–123.
4. Millán, J.L. The Role of Phosphatases in the Initiation of Skeletal Mineralization. *Calcified Tissue International* 2013, *93*, 299–306. DOI: 10.1007/s00223-012-9672-8
5. Millán, J.L.; Whyte, M.P. Alkaline Phosphatase and Hypophosphatasia. *Calcified Tissue International* **2016**, *98*, 398–416. DOI: 10.1007/s00223-015-0079-1
6. Makris, K.; Mousa, C.; Cavalier, E. Alkaline phosphatases: Biochemistry, functions, and measurement. *Calcif. Tissue Int.* **2023**, *112*, 233–242. DOI: 10.1007/s00223-022-01048-x
7. Minisola, S.; Cipriani, C.; Colangelo, L.; Labbadia, G.; Pepe, J.; Magnusson, P. Diagnostic Approach to Abnormal Alkaline Phosphatase Value. *Mayo Clinic Proceedings* **2025**, *100*, 712–728. DOI: 10.1016/j.mayocp.2024.11.019
8. Sharma, U., Pal, D., & Prasad, R. (2014). Alkaline phosphatase: an overview. *Indian journal of clinical biochemistry*, **2014**, *29*(3), 269-278. DOI: 10.1007/s12291-013-0408-y
9. McKenna, M.J.; Hamilton, T.A.; Sussman, H.H. Comparison of human alkaline phosphatase isoenzymes: structural evidence for three protein classes. *Biochem. J.* **1979**, *181*, 67–73. DOI: 10.1042/bj1810067
10. Mornet, E.; Stura, E.; Lia-Baldini, A.-S.; Stigbrand, T.; Ménez, A.; Le Du, M.-H. Structural evidence for a functional role of human tissue nonspecific alkaline phosphatase in bone mineralization. *J. Biol. Chem.* **2001**, *276*, 31171–31178. DOI: 10.1074/jbc.M102788200
11. Drechsler, C.; Verduijn, M.; Pilz, S.; Krediet, R.T.; Dekker, F.W.; Wanner, C.; Ketteler, M.; Boeschoten, E.W.; Brandenburg, V. Bone Alkaline Phosphatase and Mortality in Dialysis Patients. *Clin. J. Am. Soc. Nephrol.* **2011**, *6*, 1752–1759. DOI: 10.2215/CJN.10091110
12. Haarhaus, M.; Monier-Faugere, M.-C.; Magnusson, P.; Malluche, H.H. Bone Alkaline Phosphatase Isoforms in Hemodialysis Patients with Low versus Non-Low Bone Turnover: A Diagnostic Test Study. *Am. J. Kidney Dis.* **2015**, *65*, 123–132. DOI: 10.1053/j.ajkd.2015.02.323
13. Roston, D.; Cui, Q. Substrate and Transition State Binding in Alkaline Phosphatase Analyzed by Computation of Oxygen Isotope Effects. J. Am. Chem. Soc. 2016, 138, 11946–11957. DOI: 10.1021/jacs.6b07347
14. Igunnu, A.; Singh, J.; Flanagan, J.U. Distinct Metal Ion Requirements for the Phosphomonoesterase and Phosphodiesterase Activities of Calf Intestinal Alkaline Phosphatase. *Open Biochem. J.* **2011**, *5*, 67–75. DOI: 10.2174/1874091X01105010067

 doi:10.20944/preprints202511.2139.v1

15. Marhuenda-Egea, F.C.; Piera-Velázquez, S.; Cadenas, C.; Cadenas, E. Kinetic Regulation of an Alkaline *p*-Nitrophenylphosphate Phosphatase from *Halobacterium salinarum* in Low Water System by Mn^{2+} and Monovalent Cations. *FEMS Microbiol. Lett.* **2001**, *198*, 111–115. DOI: 10.1111/j.1574-6968.2001.tb10627.x
16. Holtz, K.M.; Kantrowitz, E.R. The mechanism of the alkaline phosphatase reaction: insights from NMR, crystallography and site-specific mutagenesis. *FEBS Lett.* **1999**, *462*, 7–11. DOI: 10.1016/S0014-5793(99)01448-9
17. Dean, R.L. Kinetic studies with alkaline phosphatase in the presence and absence of inhibitors and divalent cations. *Biochem. Mol. Biol. Educ.* **2002**, *30*, 401–407. DOI: 10.1002/bmb.2002.494030060138
18. Barth, A. Infrared Spectroscopy of Proteins. *Biochim. Biophys. Acta Bioenerg.* **2007**, *1767*, 1073–1101. DOI: 10.1016/j.bbabio.2007.06.004
19. Barth, A.; Zscherp, C. What Vibrations Tell about Proteins. *Q. Rev. Biophys.* **2002**, *35*, 369–430. DOI: 10.1017/S0033583502003815
20. Jackson, M.; Mantsch, H.H. The Use and Misuse of FTIR Spectroscopy in the Determination of Protein Structure. *Crit. Rev. Biochem. Mol. Biol.* **1995**, *30*, 95–120. DOI: 10.3109/10409239509085140
21. Goormaghtigh, E.; Ruysschaert, J.-M.; Raussens, V. Evaluation of the Information Content in Infrared Spectra for Protein Secondary Structure Determination. *Biophys. J.* **2006**, *90*, 2946–2957. DOI: 10.1529/biophysj.105.072017
22. Kumar, S.; Barth, A. Following Enzyme Activity with Infrared Spectroscopy. *Sensors* **2010**, *10*, 2626–2637. DOI: 10.3390/s100402626
23. Fabian, H.; Mäntele, W. Infrared spectroscopy of proteins. In *Handbook of Vibrational Spectroscopy*; John Wiley & Sons: Chichester, **2002**; pp 3399–3425. DOI: 10.1002/0470027320.s8201
24. Shi, H.; Lercher, J.A.; Yu, X. Sailing into uncharted waters: recent advances in the in situ monitoring of catalytic processes in aqueous environments. *Catal. Sci. Technol.* **2015**, *5*, 3035–3060. DOI: 10.1039/C4CY01720J
25. Montis, C.; Berti, D. Controlling the kinetics of an enzymatic reaction through enzyme or substrate confinement into lipid mesophases with tunable structural parameters. *Int. J. Mol. Sci.* **2020**, *21*, 5116. DOI: 10.3390/ijms21145116
26. Zhao, J.; Cui, J.-K.; Chen, R.-X.; Tang, Z.-Z.; Tan, Z.-L.; Jiang, L.-Y.; Liu, F. Real-time in-situ quantification of protein secondary structures in aqueous solution based on ATR-FTIR subtraction spectrum. *Biochem. Eng. J.* **2021**, *176*, 108225. DOI: 10.1016/j.bej.2021.108225
27. Lin-Vien, D.; Colthup, N.B.; Fateley, W.G.; Grasselli, J.G. *The Handbook of Infrared and Raman Characteristic Frequencies of Organic Molecules*; Academic Press: San Diego, CA, USA, 1991.
28. Ferraro, J.R.; Nakamoto, K.; Brown, C.W. *Introductory Raman Spectroscopy*, 2nd ed.; Academic Press: Burlington, MA, USA, 2003.
29. Nakamoto, K. *Infrared and Raman Spectra of Inorganic and Coordination Compounds*, 6th ed.; Wiley: Hoboken, NJ, USA, 2009.
30. Movasaghi, Z.; Rehman, S.; Rehman, I.U. Fourier Transform Infrared (FTIR) Spectroscopy of Biological Tissues. *Appl. Spectrosc. Rev.* **2008**, *43*, 134–179. DOI: 10.1080/05704920701829043
31. Ji Y., Yang X., Ji Z., Zhu L., Ma N., Chen D., Jia X., Tang J., Cao Y. DFT-calculated IR spectrum amide I, II, and III band contributions of N-methylacetamide fine components. *ACS omega* **2020** *5(15)*:8572-8578. DOI: 10.1021/acsomega.9b04421
32. Usoltsev, D.; Sitnikova, V.; Kajava, A.; Uspenskaya, M. Systematic FTIR Spectroscopy Study of the Secondary Structure Changes in Human Serum Albumin under Various Denaturation Conditions. *Biomolecules* **2019**, *9*, 359. DOI: 10.3390/biom9080359
33. Bonnin, S.; Besson, F.; Gelhausen, M.; Chierici, S.; Roux, B. A FTIR Spectroscopy Evidence of the Interactions between Wheat Germ Agglutinin and N-Acetylglucosamine Residues. *FEBS Lett.* **1999**, *456*, 361–364. DOI: 10.1016/S0014-5793(99)00981-3
34. WebSpectra. IR Absorption Table. 2000. Available online: https://webspectra.chem.ucla.edu/irtable.html (accessed on 1 October 2025).
35. Vidal, B. de C.; Mello, M.L.S. Collagen Type I Amide I Band Infrared Spectroscopy. *Micron* **2011**, *42*, 283–289. DOI: 10.1016/j.micron.2010.09.010

 doi:10.20944/preprints202511.2139.v1

36. Wang, Y.; Xu, K.; Li, Y.; Feng, Q. Fourier transform infrared spectroscopy analysis of the active components in serum of rats treated with Zuogui Pill. *J. Tradit. Chin. Med. Sci.* **2015**, *2*, 264–269. DOI: 10.1016/j.jtcms.2016.01.006
37. Smith, B.C. The carbonyl group, part V: Carboxylates—coming clean. Spectroscopy Online 2018. Available at: https://www.spectroscopyonline.com/view/carbonyl-group-part-v-carboxylates-coming-clean
38. Chia, N.C.; Mendelson, R. Conformational disorder in unsaturated phospholipids by FTIR spectroscopy. *Biochim. Biophys. Acta* **1996**, *1283*, 1–8. DOI: 10.1016/0005-2736(96)00095-8
39. Jastrzębski, W.; Sitarz, M.; Rokita, M.; Bułat, K. Infrared spectroscopy of different phosphates structures. *Spectrochim. Acta A Mol. Biomol. Spectrosc.* **2011**, *79*, 722–727. DOI: 10.1016/j.saa.2010.08.044
40. Linstrom, P.J.; Mallard, W.G., Eds. *NIST Chemistry WebBook*, NIST Standard Reference Database Number 69; National Institute of Standards and Technology: Gaithersburg, MD, USA. Available online: https://webbook.nist.gov/chemistry/ (accessed on 1 October 2025).
41. OrgChemBoulder. *IR Spectroscopy Tutorial*; University of Colorado Boulder, Department of Chemistry and Biochemistry. Available online: https://orgchemboulder.com/Spectroscopy/irtutor/tutorial.shtml (accessed on 1 October 2025).
42. LibreTexts. Infrared Spectroscopy. *Chemistry LibreTexts*. Available online: https://chem.libretexts.org/Bookshelves/Physical_and_Theoretical_Chemistry_Textbook_Maps/Supplemental_Modules_%28Physical_and_Theoretical_Chemistry%29/Spectroscopy/Vibrational_Spectroscopy/Infrared_Spectroscopy (accessed on 1 October 2025)
43. Socrates, G. *Infrared and Raman Characteristic Group Frequencies: Tables and Charts*; 3rd ed.; Wiley: Chichester, UK, 2001.
44. Larkin, P. *Infrared and Raman Spectroscopy: Principles and Spectral Interpretation*; 2nd ed.; Elsevier: Amsterdam, The Netherlands, 2018.
45. Abkowicz-Bieńko, A.J.; Latajka, Z.; Bieńko, D.C.; Michalska, D. Theoretical infrared spectrum and revised assignment for *para*-nitrophenol: density functional theory studies. *Chem. Phys.* **1999**, *250*, 123–129. DOI: 10.1016/S0301-0104(99)00296-7
46. Koleva, V.; Stefov, V.; Cahil, A.; Najdoski, M.; Šoptrajanov, B.; Engelen, B.; Lutz, H.-D. Infrared and Raman studies of manganese dihydrogen phosphate dihydrate, $Mn(H_2PO_4)_2{\cdot}2H_2O$. **Part I**: Region of the vibrations of the phosphate ions and external modes of the water molecules. *J. Mol. Struct.* **2009**, *917* (2–3), 117–124. DOI: 10.1016/j.molstruc.2008.07.002
47. Sun, S. T.; et al. Microhydrated dihydrogen phosphate clusters probed by gas phase vibrational spectroscopy and first principles calculations. *Phys. Chem. Chem. Phys.* **2015**, *17*, 25714–25724. DOI: 10.1039/C5CP02253C